

# Open-loop phase shifting for fast acquisition of interferograms in low light levels

Tyler M. McCracken,<sup>1,\*</sup> Colby A. Jurgenson,<sup>3</sup> Chris A. Haniff,<sup>2</sup> David F. Buscher,<sup>2</sup> John S. Young,<sup>2</sup> and Michelle Creech-Eakman<sup>1</sup>

<sup>1</sup>Magdalena Ridge Observatory Interferometer, New Mexico Institute of Mining and Technology, 801 Leroy Place, Socorro, New Mexico 87801, USA

<sup>2</sup>Cavendish Laboratory, Astrophysics Group, University of Cambridge, JJ Thomson Avenue, Cambridge CB3 0HE, UK

<sup>3</sup>Astronomy Department, Yale University, 260 Whitney Avenue, New Haven, Connecticut 06511, USA

\*Corresponding author: [tmccracken@mro.nmt.edu](mailto:tmccracken@mro.nmt.edu)

Received 15 April 2013; revised 6 June 2013; accepted 6 June 2013;  
posted 7 June 2013 (Doc. ID 188756); published 9 July 2013

Phase shifting interferometry relies on sets of interferograms taken at multiple known phase offsets to deduce the instantaneous phase of a quasi-static fringe pattern. The traditional method for introducing these phase shifts has been either to step a mirror, and measure the fringe pattern at each step, or to scan a mirror, integrating the fringe pattern for discrete time intervals while the fringes “move” on the detector. A stepping mirror eliminates this fringe smear but has typically required a closed-loop controller to ensure that the optical path introduced is accurately known. Furthermore, implementing rapid stepping of a moderately sized optic can prove difficult if the fringe phase needs to be measured on a short time scale. We report results demonstrating very fast ( $>100$  Hz) and precise phase shifting using a piezomodulated mirror operated in open-loop without any position feedback. Our method exploits the use of a synthetic driving waveform that is optimized to match the complex frequency response of the modulator and its supported optic. For phase measurements in the near-infrared at  $2.15\ \mu\text{m}$ , and with a time between steps as small as  $0.2$  ms, we report errors below  $\lambda/100$  in the desired position of our optic, i.e., an effective optical path difference error of  $\sim\lambda/55$ . For applications in near-infrared stellar interferometry, this implies an enhancement in the fringe-tracking sensitivity of roughly 20% (in the photon-limited regime) over that which is conventionally realized using a swept mirror. © 2013 Optical Society of America

*OCIS codes:* (120.0120) Instrumentation, measurement, and metrology; (120.5050) Phase measurement; (120.5060) Phase modulation; (120.3180) Interferometry.

<http://dx.doi.org/10.1364/AO.52.004922>

## 1. Introduction

Phase shifting interferometry (PSI) seeks to determine the phase of a fringe pattern by measuring the fringes multiple times, when several known optical path offsets (centered on some initial optical path difference, OPD) are introduced into one of the interfering beams. The fringe amplitude and phase are then estimated from these measurements via what

is essentially a discrete Fourier transform. Traditionally, these optical path, or phase, shifts have been introduced by using piezoelectric transducers (PZTs) either as optical fiber stretchers [1] or as devices to mechanically scan or step a small mirror.

When using PZTs as precision positioning devices, the nonlinearity of their response has been a continual issue. These nonlinearities can arise because of, for example, the excitation of harmonics, hysteresis in the response, and creep. To avoid the unintended excitation of harmonics and achieve stable phase

shifts, PZTs are generally driven well below their resonant frequency, limiting the speed with which large amplitude motions can be commanded. Hysteresis and creep are commonly corrected for by using closed-loop controllers which, for high bandwidths, generally require sophisticated equipment for the feedback control loop [1–3]. Even with such specialized equipment, these implementations are rarely able to secure series of interferograms at rates higher than 50 Hz when discrete optical path steps are required.

An additional complication of closed-loop schemes used in laboratory settings is that they may use some of the light from the fringe pattern to determine their error signal. Thus, in applications where these photons are at a premium, e.g., in stellar interferometry, this can lead to a reduction in the optical signal available for astrophysical study and so is not a desirable solution strategy.

Methods for delivering precision positioning with PZTs when used in open-loop have been proposed. These methods account for the creep by modeling it as a logarithmic term [4] and mitigate hysteresis by adding a quadratic phase term [5] to the position set by a voltage. While these solutions have been moderately successful, they do not address the desire to realize phase modulation at high bandwidths, nor is it clear how frequently these corrections need to be tuned to maintain good performance.

An obvious strategy for managing the nonlinearities in a typical PZT/optomechanical setup would be to drive the device with a synthetic voltage waveform tuned deliberately in order to realize the appropriate periodic motion. This would be based on a Fourier decomposition of the desired motion, but would be optimized so as to, for example, not excite resonances and compensate for the dynamics of the specific optomechanical arrangement used to mount the optic to the modulator and the modulator to the interferometric experiment.

We report here on results obtained using such a system in which an “optimized” waveform has been used to step a small mirror in a typical PSI setup. Measurements taken with an external metrology system show that the typical errors in positioning, when operating with a PSI cycle time of 7.5 ms and steps of order 250 nm, are less than a few tens of nanometers, and are dominated by the mechanical resonances of our mounts. Strain gauge measurements of the PZTs themselves show positioning errors (relative to the mirror mount) some ten times smaller. Our implementation is relatively low cost, and we demonstrate that it is repeatable and stable for an extended period of time.

In Section 2 we introduce our phase shifting scheme, and outline the requirements pertaining to our desired stellar interferometry application. The details of our setup and the algorithm used to obtain an optimized waveform are presented in Section 3. Our results of the optimization process are shown in Section 4 and are followed in Section 5

by a discussion of the impact an optimized modulation scheme has on the observables of a stellar interferometer.

## 2. Stellar Interferometers and Phase Shifting Interferometry

One application of PSI is in stellar interferometry and, specifically, the fringe tracking methods used to stabilize the path lengths between the separate telescopes collecting light in the interferometric array [6]. Stellar interferometers now operate routinely in the optical and near- and mid-infrared regimes, and the most critical technology driver for them is the desire to observe increasingly fainter targets. Because ground-based arrays operate beneath the Earth’s turbulent atmosphere, all high-sensitivity arrays exploit so-called fringe-tracking subsystems to monitor and compensate for the atmospheric perturbations, and hence stabilize the path lengths between the different telescopes in the array. The atmospheric path perturbations are typically sensed by measuring the instantaneous phase of the stellar interference fringes using PSI. The ability to monitor these perturbations in real time is the main determinant of the interferometer’s limiting magnitude, that is, how faint a target it can observe [7].

Not surprisingly, for faint, and hence interesting, targets, most stellar interferometers operate in a photon-starved environment. Furthermore, the typical time scale for significant atmospheric perturbations—the so-called coherence time,  $t_0$ —is very small. For example, in the near-infrared  $K$ -band window centered at 2.2  $\mu\text{m}$ ,  $t_0$  is roughly 20 ms under moderate atmospheric conditions. This combination of intrinsically faint targets and a short time scale on which to make measurements of the stellar fringe patterns is a major technical challenge for astronomical interferometrists.

As mentioned above, astronomical fringe tracking algorithms rely heavily on PSI to determine the phases of the stellar fringe patterns. Once determined, these phases are converted to OPDs, and these can be introduced into the light paths within the interferometer by using actuated components. Frequently, the interferometer’s delay lines, which are also responsible for correcting the variable geometric delay due to earth rotation, perform this function, but other smaller adjustable components can be used.

In most astronomical implementations, PSI is usually implemented by continuously scanning a small mirror in a triangle or sawtooth waveform with a peak-to-peak amplitude of one (or a few) waves, rather than stepping the mirror to one of four positions. Other methods for determining the fringe offset using much longer strokes exist but these are not considered here [8,9]. Typically, a continuous linear scan with a range of one wavelength is divided into four equal sections, and the temporally modulated stellar fringes are integrated on a detector for these

four consecutive time periods. The resulting intensity measurements are subsequently used to recover the fringe amplitude and phase. This procedure is frequently referred to as the ABCD method, where the letters A, B, C, and D conventionally refer to the four sequential intensity measurements.

It is possible to introduce the ABCD phase steps simultaneously, by splitting the interfering beams four ways, and using four separate beam combiners, each with its own appropriate static OPD. This alternative approach has been taken at the Very Large Telescope Interferometer's (VLTI's) PRIMA instrument [10,11], but since it requires additional splitting and recombining optics and detectors, it has not been favored for interferometers where fringe tracking on multiple baselines is desirable. Examples of fringe tracking engines that have utilized the temporal ABCD scheme include CHARA's Classic [12] and CHAMP [13] instruments, VLTI's FINITO [14] fringe tracker, the Navy Prototype Optical Interferometer's (NPOI's) fringe tracker [15], the Keck Interferometer's FATCAT [16,17], and the Palomar Testbed Interferometer fringe tracker [18].

While all of these latter instruments have been able to track fringes while scanning at upwards of 500 Hz, none of them have addressed the issue of the fringe smear and ultimately the decrease in sensitivity incurred by integrating the fringe signal during the scanning motion. Much effort has gone into characterizing the biases and signal-to-noise ratio penalties incurred when using continuous motion [19], and other studies have focused on the impact of nonlinearities seen when operating PZTs [20,21]. However, it would clearly be beneficial if discrete and fast phase stepping were possible in a temporally modulated instrument.

The Magdalena Ridge Observatory Interferometer (MROI) [22], currently under construction in southern New Mexico, aims to use a dedicated fringe tracker with phase stepping provided by PZT stages. This fringe tracker, named the Infrared Coherencing

Nearest Neighbor tracker or ICoNN [23], will operate in the astronomical  $H$  (1.49 to 1.78  $\mu\text{m}$ ) and  $K_S$  (1.99 to 2.31  $\mu\text{m}$ ) bands and is required to allow the measurement of four phase-shifted interferograms, using  $\pi/2$  steps, within a total time of 5 ms. More specifically, one of its modes will employ step pyramid modulation of the optical path.

This modulation scheme is depicted schematically in Fig. 1, which shows the planned mirror position, together with the activity of the fringe detector, as a function of time for a typical modulator unit. In this scheme, the mirror is stepped between four possible locations and is held stably at each one, during which time the detector integrates the signal and then is rapidly stepped to a new position. Multiple non-destructive reads of the detector signal at intervals  $T_{\text{read}}$  can be made during the integration times,  $T_{\text{int}}$ , while the signal that accumulates on the detector during the motion between each mirror position can be easily discarded. The goals are to maximize the hold time at each location, to minimize the slewing time between mirror positions, and to allow a cycle of four interferograms to be recorded in no more than 5 ms.

The optical architecture of ICoNN is such that two complementary outputs,  $180^\circ$  out of phase, can be measured simultaneously on separate detectors. In the language of the ABCD scheme, when the modulator is at its starting position, one detector will measure A, and the other C; while when the modulator is at its first stepped position, the two detectors will measure the B and D contributions. The two subsequent modulator positions (identified as 2 and 3 in Fig. 1) allow the same four measurements to be made again, though with the detectors exchanged so as to allow for correction of their individual sensitivities and any throughput mismatches from beam combiner output to detector.

The size of each modulator step,  $D_{\text{mod}}$ , will be determined by the beam combiner architecture and the bandpass of the light being interfered. In the ICoNN

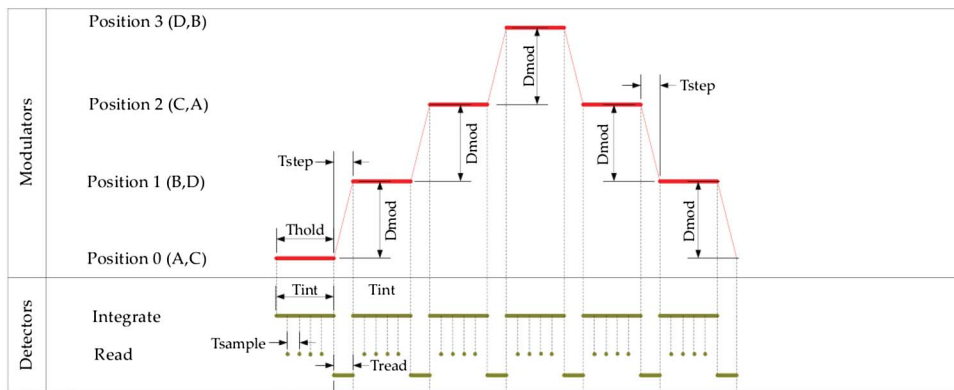


Fig. 1. Diagram depicting the envisioned step pyramid OPD modulation scheme at the MROI. Each position change corresponds to a  $\pi/2$  phase shift in the fringe pattern, which requires an OPD step of  $D_{\text{mod}}$ . During  $T_{\text{hold}}$ , the fringe detector integrates signal for a period  $T_{\text{int}}$ , and during this time the fringe detectors will have the ability to nondestructively sample their pixels multiple times on a timescale  $T_{\text{sample}}$ . These detector reads are discarded during the time  $T_{\text{step}}$  during which time the modulator is stepped to the next measurement point. Thereafter the cycle repeats, in that during subsequent  $T_{\text{hold}}$ s the detectors continue to integrate signal and are multiply read. To allow four interferograms to be recorded in 5 ms,  $T_{\text{hold}}$  can at most be 1.25 ms, while  $T_{\text{step}}$  should be as short as possible.

tracker the optical layout will use mirrors with an angle of incidence of  $15^\circ$ , and so the OPD introduced by a mirror motion of  $x(t)$  will be

$$\text{OPD}(t) = 2x(t) \cos(15^\circ). \quad (1)$$

For a  $\pi/2$  phase shift, this corresponds to values of  $D_{\text{Mod}}$  of 200 and 260 nm for measurements in the near-infrared  $H$  band ( $1.65 \mu\text{m}$ ) and  $K_S$  band ( $2.15 \mu\text{m}$ ). These values are strictly appropriate only for the central wavelengths of each bandpass, and so the other wavelengths within the bandpass will experience either a slightly greater or lesser phase shift.

The two primary difficulties in realizing the envisioned modulation scheme depicted in Fig. 1 are how to drive the modulator fast enough and how to be sure of the position of the modulator in real time without using additional optics or sensing systems. In addition, reaching a stable mirror position requires sufficient settling time for the modulator, which can impose a significant lower limit on  $T_{\text{step}}$ .

Closed-loop controllers require continuous computing power and feedback from some form of a motion monitor. Typical methods of monitoring motion in the laboratory have involved the use of independent metrology systems or, having picked off some of the signal itself, the use of additional sensitive and fast readout cameras. In some stellar interferometric implementations, the modulated mirrors have been mounted within the instruments' delay lines (e.g., see [24]) and in these cases it has been possible to utilize the laser metrology systems associated with the delay lines themselves to monitor the OPD introduced. A different approach is to use strain gauges attached directly to the modulating PZT elements. However, these are inherently noisy devices and would likely require specialized controllers to reach the  $\sim 5$  kHz sampling frequency needed to support a value for  $T_{\text{hold}}$  as small as 1.25 ms [25].

For the MROI application, where low light levels will be typical and where up to nine beamlines will need to be modulated simultaneously, we have been investigating alternatives to the active solutions outlined above. More specifically, we have converged on an approach where an iterative algorithm is used to determine a suitable synthetic driving waveform that will allow our modulators to be run in open-loop, ideally for whole nights without retuning.

### 3. Experimental Setup

Our experimental setup in the lab, which emulates the system that we envision deploying at the MROI, is a standard phase shifting scheme based on PZT modulators. Two collimated beams of light from an artificial source (a proxy for the celestial target at MROI) are fed to the ICoNN beam combiner, and the interference signal is detected as a function of the differential optical path between the beams. User-defined OPDs are introduced by reflection of

one of the beams off a plane mirror mounted on a modulator. We seek to optimize the periodic OPD modulation without closed-loop control of the mirror motion and the real-time monitoring of the mirror position this would entail. It is the stability and precise form of this open-loop modulation that our new implementation demonstrates.

#### A. Hardware

The hardware used to realize the open-loop modulation is shown schematically in Fig. 2 and represents the minimal amount of hardware one would need for our temporal phase modulation scheme.

In our setup a DAQ card, the Innovative Integration X3-Servo, which has simultaneous sampling analog-to-digital converters (ADCs) and digital-to-analog converters (DACs), was installed in a personal computer to synthesize the driving waveform. The synthesized waveform was then conditioned and fed to the modulator. We used a Piezomechanik STr-35/150/6, designed for mirror shifting applications and packaged with a built-in strain gauge for position monitoring. This device had a measured stroke of  $9 \mu\text{m}$  and a manufacturer-quoted resonant frequency of 10 kHz. It consists of three PZTs mounted in parallel acting as a tripod support, which move the mounted mirror [26]. There is no balancing PZT, that is, no PZT driven in the opposite direction to minimize mechanical vibrations. The strain gauge signal from the modulator was amplified with a Piezomechanik DMS series strain gauge amplifier and sampled with an ADC on the DAQ card. No noise filters were used except for the 400 kHz anti-aliasing filter built into the ADCs on the DAQ card.

Waveform conditioning involved first amplification and power boosting with an inverting amplifier, an Apex MP108, and then offsetting by 75 V so as to center the signal within the modulator's operating range (0–150 V). A biased high-pass filter was used, with the lower cutoff frequency of the filter set to  $\sim 1$  Hz. Power boosting was necessary to allow rapid

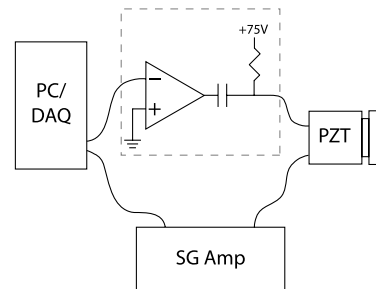


Fig. 2. Schematic diagram of the hardware used to realize the OPD modulation scheme. The modulation waveform is generated by a personal-computer (PC)-based DAQ card. The waveform is amplified and power boosted using an inverting amplifier, then offset with a biased high-pass filter before driving the modulator (PZT). The modulator's strain gauge (SG) signal is amplified then sampled by the DAQ card. The dashed box represents hardware specific to the modulator used. The remaining hardware is general to other modulation schemes and could be tailored for other setups.

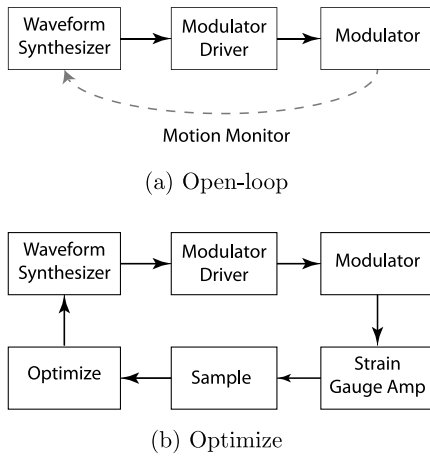


Fig. 3. Block diagrams for the two modes of modulator operation. (a) In the open-loop mode, the modulator is run with only a means to sense its motion via the strain gauge. No feedback is employed: the dashed arrow labeled “Motion Monitor” simply reflects the fact that the modulator motion can be logged for postexperiment analysis. (b) Block diagram for creating an optimized waveform. The strain gauge is sampled, and the driving waveform optimized in an iterative manner as described in the text.

movement of the mirror optic at the stepping and turnaround points of the modulation cycle.

Independent calibration of the built-in strain gauge was performed with an external commercial laser metrology system. The details of the calibration process are presented in Section 4, but a simple scaling factor of strain gauge position signal to mirror motion (nanometers per volt) was found to be adequate to describe the actual motion of the driven optic.

The modulator could be run in one of two modes: an open-loop operational mode [Fig. 3(a)] and the waveform optimization mode [Fig. 3(b)]. When operated in open-loop mode, an ADC on the DAQ card was available to sample the strain gauge signal at any time, but this simply served to monitor the optic motion while fringes were being recorded.

The optimization mode was used to iteratively seek a synthetic waveform that gave the correct open-loop OPD modulation. In this mode both a DAC and an ADC were sampled simultaneously for approximately one second while the mirror was being driven. After each second of data had been accumulated, an iteration of the algorithm was applied to modify the driving waveform based on the response measured by the strain gauges and the desired OPD modulation. A further data sequence was then captured, and another modification of the drive waveform performed. These operations were repeated until the measured response had converged to the desired modulation.

## B. Optimization Process

The detailed procedure used to optimize the driving waveform sent to the PZT modulator was as follows.

First, the desired periodic OPD modulation scheme was expressed as a truncated Fourier series

using the first  $N$  coefficients,  $T_N$  of the full expansion. The initial driving waveform  $d_N(t)$  was then set equal to this truncated Fourier series, and a time series of the resulting modulator position,  $r_N(t)$ , was recorded by the strain gauge. A high signal-to-noise ratio version of this recording, averaged over a few hundred cycles, was then decomposed into its Fourier components, and the complex response coefficients,  $R_N$  (that is, the Fourier coefficients seen in the *actual* strain-gauge-sensed motion), were recovered. Our setup, which had the DAC and ADC clocked from the same source, permitted us to easily sample an integer number of periods of  $r_N(t)$ , making extraction of the  $R_N$  relatively straightforward.

Once the set of complex  $R_N$  had been extracted, the driving coefficients  $D_N$  were adjusted by using the optimization algorithm described in [27]. For the first iteration, the driving coefficients were adjusted based on the difference between the target coefficients and the measured response:

$$D_{N,1} = T_N + g(T_N - R_{N,0}), \quad (2)$$

where  $g$  denotes a gain value, which we set to 0.3.

On subsequent iterations, the driving coefficients were adjusted slightly differently according to the following scheme:

$$D_{N,k+1} = D_{N,k} + g(T_N - R_{N,k}) \left( \frac{D_{N,k} - D_{N,k-1}}{R_{N,k} - R_{N,k-1}} \right), \quad (3)$$

where  $k$  denotes the iteration number. To trap division by zero in the final term of the updating scheme, all  $N$  coefficients in  $R_{N,k}$  were checked against the corresponding coefficient from the previous iteration, i.e.,  $R_{N,k-1}$ . If any of the current and previous response coefficients were sufficiently close to each other, the coefficient  $D_{N,k+1}$  was set to  $D_{N,k}$ , and that specific coefficient was deemed to have been optimized. The updated driving waveform  $d_{N,k+1}(t)$  was then generated from the  $D_{N,k+1}$ , and the process of remeasurement of the resulting mirror motion and driving coefficient adjustment repeated until the algorithm converged [27].

The level of convergence was assessed by examining the standard deviation of the difference between the (finite-series) target waveform and the measured modulator response:

$$\sigma_{\text{conv}} = \text{STDEV}(t_N(t) - x_N(t)), \quad (4)$$

where  $x_N(t)$  is the reconstructed strain gauge signal comprised of  $R_{N,k}$ . A range of gains were explored,  $0.1 \leq g \leq 0.3$ , and it was found that, by increasing the gain, the algorithm required fewer iterations to achieve the same level of convergence. A modest value of 0.3 was adopted, which provided an optimized waveform in 25 iterations or just over 2 min [the majority of this time was used to sample  $r_N(t)$ ]. Increasing the gain from 0.1 to 0.3 decreased

the convergence time by only a few iterations, each of which took approximately 5 s to record and analyze.

#### 4. Results

We present results here for two typical waveforms appropriate for low-light level stellar interferometry PSI applications, a triangle wave and a step pyramid. The waveform amplitudes were chosen such that the induced phase shift would correspond to taking interferograms at phase intervals of  $\pi/2$  in the 2.15  $\mu\text{m}$  near-infrared  $K_S$  band. This corresponds to a peak-to-peak amplitude of 1040 nm for the triangle wave and a step size of 260 nm for the step pyramid.

Obtaining reliable results from the optimization algorithm required accurate calibration of the strain gauge to mirror motion (volts to nanometers). The calibration of the strain gauge was undertaken using an HP 5518A laser metrology system, which was used to monitor the position of the front surface of the modulated optic. The metrology system had a position accuracy of 5 nm and was sampled with an Agilent E1735A USB axis module. Initial calibration was done by driving the modulator with a 100 Hz sine wave of fixed amplitude (of roughly 100 nm amplitude) and sampling the resulting motion with the laser metrology system and strain gauge simultaneously. The conversion factor of volts to nanometers for the strain gauge was then determined by comparing the amplitudes of the two signals. Similar calibrations made at 300 and 500 Hz gave scale factors that were very slightly smaller, by a few percent. At higher odd multiples of 100 Hz up to 2 kHz the conversion factors showed much more variation, by as much as  $\pm 10\%$ , but the much smaller relative contribution of these Fourier components in the drive waveform should have moderated these effects. Once an optimized driving waveform had been obtained, the calibration was cross checked by remeasuring the mirror motion with the HP laser metrology system and comparing its motion to that derived from the strain gauge data and the driving waveform coefficients. Typical inconsistencies between the conversion factors determined in these two ways were less than 5%.

##### A. Frequency Response and Number of Coefficients

A top level requirement for our astronomical application was to secure four phase shifted interferograms within 5 ms. To satisfy this requirement, we aimed to realize the triangle wave modulation with a base frequency of 100 Hz and the step pyramid modulation with a base frequency of 133 Hz. This difference in base frequency arises because the triangle samples interferograms 1 and 4 (corresponding to positions 0 and 3 in Fig. 1) twice per period, while the step pyramid samples interferograms 1 and 4 only once per period.

Prior to optimization, the frequency response of our PZT/optic/mechanical assembly was mapped from 20 Hz to 10 kHz to identify any optomechanical

resonances and hence warn us of any specific frequencies that we might need to suppress in any optimized driving waveform. This frequency response is shown in Fig. 4. Up to around 3 kHz the response is smooth and slowly varying, whereas above this frequency the response varies more rapidly with frequency, and there are multiple points of resonance and antiresonance. We found that, with the exception of a few very specific frequencies corresponding to the largest resonances, the modulator could be driven sinusoidally at frequencies of up to about 6 kHz with no obvious problems.

The observed frequency response was used to aid in determining the upper limit on  $N$ , the number of coefficients to use in the optimized PZT drive waveform. Since the Fourier decomposition of a triangle wave only includes odd coefficients whose amplitude scales as  $1/n^2$ , very few terms are necessary to generate an accurate representation of a triangular waveform. For this modulation scheme, we set  $N$  equal to 32, implying a total bandwidth of 3.2 kHz (i.e.,  $32 \times 100$  Hz) in order to keep all the driving frequencies within the smooth portion of the frequency response curve.

The step pyramid modulation function proved more challenging. The Fourier decomposition of a simple square wave similarly includes only odd coefficients, but these scale much more slowly as  $1/n$ . Increasing the number of coefficients in the step pyramid drive waveform would thus be expected to reduce the ringing at each step and shorten the time taken to move between steps. However, given the frequency response of our hardware, higher-frequency harmonics are much more likely to induce unwanted resonances. As a result, to minimize the ringing and step time, the number of coefficients for the step pyramid was determined experimentally.

Optimized drive waveforms were determined for a range of different values of  $N$ , and in each case the RMS difference between the measured OPD and that

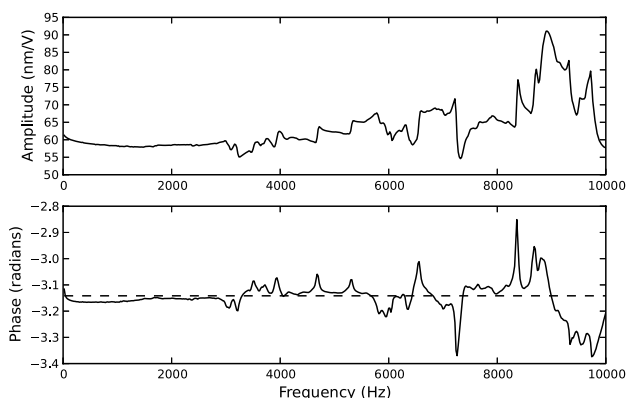


Fig. 4. Frequency response of the modulator, drive electronics, and optomechanics from 20 Hz to 10 kHz. The modulator used had a manufacturer-specified resonant frequency of 10 kHz. Up to approximately 3 kHz the response is smooth, while from 3 to 10 kHz there are multiple points of resonance and antiresonance. The phase is centered about  $-\pi$  (dashed line in the lower panel), as the conditioning circuitry uses an inverting amplifier.

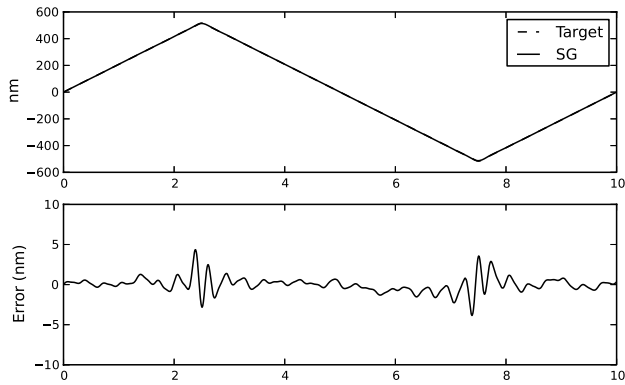


Fig. 5. Mirror motion as inferred from strain gauge data for the triangle waveform at 100 Hz for the  $K_S$  band. The strain gauge data is plotted over the target triangular wave with the difference between the waveforms shown in the lower panel. The difference plot has  $\sigma = 0.9$  nm.

expected for a perfect (i.e., using an infinite term) Fourier expansion was computed. We found that use of 45 coefficients (corresponding to a bandwidth of roughly 6 kHz) minimized this measure of misfit: fewer coefficients gave more ringing on the steps, while more coefficients resulted in modulator resonances.

When the spectrum of the error signal (as measured by the laser metrology system) was examined, the largest contributions, by a factor of three, were traced back to the 25th and 33rd coefficients alone, at frequencies of 3.325 and 4.389 kHz respectively. These coefficients were subsequently dropped from the series expansion with no further impact on performance. We believe the overall quality of the OPD modulation delivered was ultimately constrained by the design of our optomechanics, since measurements of the mirror motion as inferred from the strain gauges did not show these large harmonic contributions. As a result, we expect that improved modulation performance could in principle be delivered by using the same PZT but with a more carefully designed mechanical mount.

### B. Optimization

For waveform optimization, the algorithm was iterated until further iterations showed no improvements above the noise. This was explored experimentally, and we found that a satisfactory level of convergence was seen after 15 iterations for the triangular waveform and 25 iterations for the step pyramid.

The resulting mirror motions arising for the triangle wave and step pyramid schemes are shown in Figs. 5 and 6, respectively. The figures show the mirror motion as inferred by the on-device strain gauge (so these data do not include any contributions from mechanical resonances of the mirror mount optomechanics) plotted together with their respective truncated Fourier series. In the upper panels the target and measured data lie very close to each other, and so the lower panel in each figure shows the

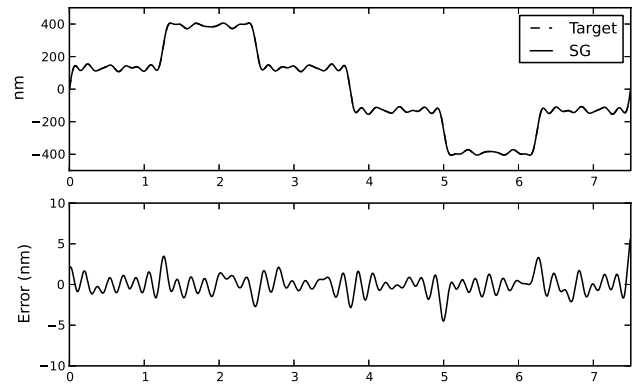


Fig. 6. Step pyramid mirror motion at 133 Hz for the  $K_S$  band as determined by strain gauge measurements. The strain gauge data are plotted together with the motion predicted on the basis of the truncated Fourier series. As before, the strain gauge data match the target motion very well, and so the lower panel more clearly shows the difference between the two curves (the error waveform). This has  $\sigma = 1.1$  nm.

difference between the truncated series and the strain-gauge-inferred motion. The standard deviations of the error plots are 0.9 nm for the triangle waveform and 1.1 nm for the step pyramid, i.e., roughly at a level of  $\lambda/1000$  for the design wavelength.

Typically, the strain gauge response deviated from the truncated Fourier expansion of the target waveform only at the inflection points for the triangle wave and the stepping points for the step pyramid modulation scheme. This is consistent with the idea that at these times the conditioning circuitry struggles most to deliver the current spikes needed to quickly and precisely move the modulator. Nevertheless, these deviations had amplitudes of at most 5 nm, and so were always very small fractions of a wavelength.

### C. Metrology Measurements

Previous implementations of PSI in stellar interferometry have frequently utilized momentum balanced PZTs [24] so as to reduce the possibility of exciting mechanical resonances when an optic is modulated rapidly. In view of the lack of such compensation in our laboratory setup, independent measurements of the mirror position were also made with our external laser interferometer.

Single modulation sweeps measured with the laser metrology system for the optimal triangle and stepped-pyramid drive waveforms for  $K_S$  band measurements are shown in Figs. 7 and 8. These figures have the same format as Figs. 5 and 6, with the upper panels showing the full-scale target and measured data, and the lower presenting the difference. The triangle wave error showed a standard deviation of around 5 nm, while the step pyramid data exhibited a larger misfit and had a standard deviation of approximately 9 nm. At some level these measurements were compromised by the quality of the interferometer system, which had a relatively poor

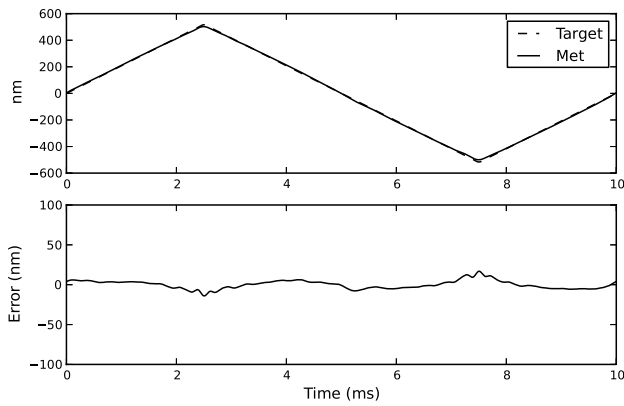


Fig. 7. Top, external metrology data for the mirror motion plotted over the target 100 Hz triangular wave OPD modulation. The lower panel shows the difference between the two waveforms plotted in the upper panel and has  $\sigma = 5.2$  nm.

resolution of only 5 nm. As such, then, our data gives an upper limit to the true errors associated with the PZT-driven OPD modulation.

Figure 7, again, reveals that the OPD error is larger near the turnaround points on the triangle wave. The metrology measures a smoother turnaround than that predicted by the target waveform, as expected for a system with finite inertia. The triangular error signal was also found to contain a 300 Hz oscillation that had an amplitude of just under 8 nm. This was not seen at all in the strain gauge data and is likely to be due to a 300 Hz mechanical vibration in our setup. When driven at base frequencies of 95 or 105 Hz, this oscillation disappeared.

The step pyramid error (Fig. 8) also showed harmonic content. Two discrete contributions—those at the 25th and 33rd harmonics—were expected, because these terms had been deliberately removed from the optimized drive waveform so as not to excite mechanical resonances. The next most significant error term was noted at the seventh harmonic ( $\sim 930$  Hz) and had an amplitude of approximately 6 nm. All the other harmonic error contributions

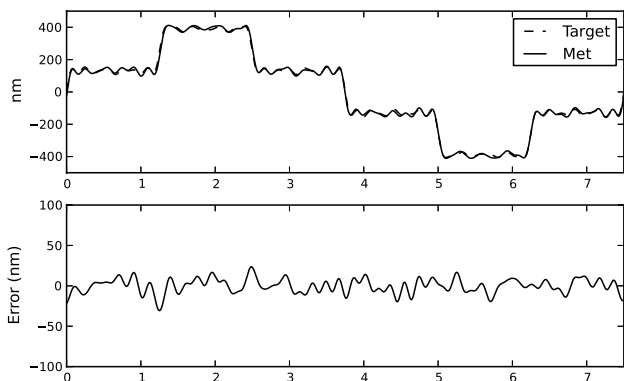


Fig. 8. Top, metrology data for the mirror motion plotted over the desired 133 Hz step pyramid motion for the  $K_S$  band. The lower panel shows the difference between the sampled metrology data and the target waveform and has  $\sigma = 8.7$  nm.

were below the 5 nm level. We note, in passing, that the mechanical mount used for these metrology measurements was not the one to be deployed in the ICoNN beam combiner, and so we expect that the mechanical vibrations present in these data will be dampened and reduced in amplitude in our final optomechanical setup. Interestingly, the residual OPD errors seen in our test setup have sizes, similar, that is, of order 5–10 nm, to those seen in typical momentum-balanced PZT modulation systems at other stellar interferometers. For example, equivalent data measured at the NPOI [28] (see lower panels of their Figs. 5 and 6) show very similar levels of OPD error in regions of the stroke far from the turnaround points.

As mentioned above, we believe the differences seen in the apparent mirror motion recorded by the strain gauge sensors and the external metrology system are most likely due to induced mechanical vibrations set up in the PZT and mirror mount. Loading of the modulator mounts with different large masses did not alter the RMS value of the OPD error significantly, but clearly moved the most significant contributor to the error from one harmonic to another. Variations in the strain gauge response as a function of frequency may also have contributed to the difference, but whatever the cause, our results confirm that, at least for the characteristic modulation strokes needed at the MROI, relatively cheap unbalanced PZT modulators can be used to introduce the desired OPD shifts with a high level of accuracy.

#### D. Stability

The stability of the optimized driving waveforms—that is, how well a driving waveform determined at some time  $T$  delivers the desired waveform at some time  $T + \Delta T$  later—is of particular interest. Little would be gained from optimizing a drive waveform if the resulting OPD modulation some time later were variable at a level that limited the utility of PSI. This would include the variability of a specific frequency's response, resulting in fringe smearing due to excessive ringing, or a change in the conversion factor of volts to nanometers resulting in a change in the overall amplitude of the OPD modulation. Such variability could be caused, for example, by temperature fluctuations in the laboratory or a change in the overall response of the modulator over its lifetime. If such variation were present, the only likely solution would be repeated reoptimization, or the installation of a separate continuous monitoring system that would check the delivered OPD modulation as time went on and signal that the response of the modulator system had altered significantly.

Long-term stability testing of the optimized drive waveforms was performed for 16 h in a standard undergraduate teaching laboratory. The time scale of our testing is consistent with the use of PSI in an astronomical scenario, where one would expect to optimize the OPD modulators at the start of a night's observing, but not repeat any calibration

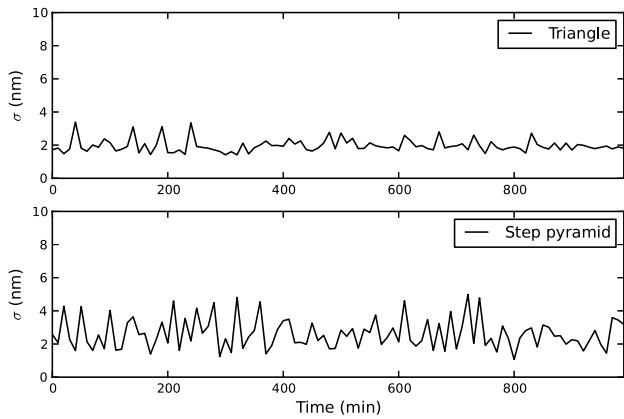


Fig. 9. RMS difference between the strain gauge and truncated series data for (top) the triangle wave and (bottom) the step pyramid modulation schemes over 16 h. The triangle wave shows an average RMS error of 2.0 nm and a 0.4 nm standard deviation. The step pyramid has an average 2.8 nm RMS error and a 0.9 nm standard deviation. No short- or long-term trends can be seen in the data, confirming good stability of the whole PZT-optic-mechanical system.

during the next 12–14 h. Tests were undertaken in a passively controlled laboratory environment, with a characteristic diurnal temperature variation of  $\pm 2^\circ\text{C}$ . Our test modulator unit was run continuously with the same optimized drive waveform, and a time series of the strain gauge data was recorded every 10 min and the mirror motion recovered.

The RMS differences between the reconstructed strain gauge signals and the truncated target series are shown as a function of time in Fig. 9. Over the 16 h testing period, no long- or short-term trends in the magnitude of the error signals were seen. The average RMS differences were 2.0 nm for the triangle wave and 2.8 nm for the step pyramid modulation, with standard deviations of 0.4 and 0.9 nm respectively. Despite the moderate temperature swings seen in the laboratory, the form of the OPD modulation delivered remained very stable. In practice, at all astronomical interferometers, the fringe tracking observations are made in temperature-stable laboratories, and so it is very unlikely that recalibration of our demonstrator during an individual night's observations would be needed.

In order to test the longer term stability of our setup, drive waveforms optimized at a given time were used to drive the modulator-optic assembly several weeks later without any reoptimization. In these cases, results similar to those shown in Fig. 9 were obtained; that is, we found no evidence for long-term (e.g., weekly) changes in the response of our PZTs. This suggests that the idea of compiling libraries of driving waveforms for different frequencies, amplitudes, and types of OPD modulation, and then picking an appropriate waveform depending on the prevailing atmospheric conditions and the desired observation wavelength, is likely to be successful and is the model we expect to adopt at the MROI.

## 5. Discussion

The results presented above suggest that the use of PSI in astronomical interferometry could be significantly enhanced through the use of true phase-stepped OPD modulation, rather than using a continuous triangular OPD scan. In astronomical interferometry the most important metric of overall system performance is the sensitivity limit of the array, and this is usually determined by the faintest target on which successful fringe tracking can be accomplished.

At low light levels, the signal-to-noise ratio (SNR) for fringe detection depends on the apparent fringe visibility,  $V$ , and the mean number of photons detected per integration,  $\langle N \rangle$ , such that  $\text{SNR} \propto V^2 \langle N \rangle$ . There are a multitude of expressions for the exact SNR depending on the design of the instrument and fringe tracking algorithm employed (e.g., see [29–31]), but in the photon-limited regime all are monotonic functions of  $V^2 \langle N \rangle$ . Thus, in order to maintain a given value of the SNR, any decrease by a factor of  $f$  in  $V$  due to instrumental deficiencies must be compensated for by an increase of  $f^2$  in  $\langle N \rangle$ . In other words, for example, a 10% drop in apparent fringe visibility would be compensated by an increase of 20% in the mean photon flux.

While the fringe visibility will be reduced by many instrumental factors, for example, spatial wavefront errors due to poor-quality optics, optical misalignments in the beam combiner, and intensity mismatches in the interfering beams, an additional contribution will arise if the fringes move during the detector integration. This is a characteristic feature of triangle wave OPD modulation, which can be almost completely eliminated if a step pyramid modulation scheme with  $T_{\text{step}} \ll T_{\text{hold}}$  can be realized.

The approximate reduction in apparent fringe visibility due to deviations in the actual OPD delivered by a modulator from that expected in a perfect stepped PSI scheme can be written as [31,32]

$$V_{\text{red}} \approx \exp\left(\frac{-\sigma_\phi^2}{2}\right), \quad (5)$$

where  $\sigma_\phi$  is the RMS difference between the actual and the desired phase, and we have assumed that (as the case for the ICoNN beam combiner) only one of the interfering beams is being modulated. Equation (5), while not exact in the general case, is appropriate as long as the RMS phase error is  $\ll 1$  rad and the frequency of the errors is a high multiple of the fringe frequency (the fundamental harmonic of the modulator). Both conditions are true in our case, as the errors introduced by the imperfect PZT stepped-pyramid modulation will have very small amplitudes compared to the wavelength of interest, and those errors are primarily at the 25th and 33rd harmonics of the fringe frequency.

For our beam combiner and modulator implementation  $\sigma_\phi$  will be given by

$$\sigma_\phi = \frac{2\pi(2\sigma_{\text{mod}} \cos(15^\circ))}{\lambda}, \quad (6)$$

where  $\lambda$  is the observing wavelength for which the optimized drive waveform has been designed and  $\sigma_{\text{mod}}$  is the mean square deviation of the optimized drive waveform signal from the desired static position. As mentioned above, the  $\cos(15^\circ)$  factor is due to the optical architecture of the ICoNN beam combiner.

Using the metrology measurements shown in Fig. 8 for the step pyramid ( $\sigma_{\text{mod}} = 8.7$  nm), and assuming that the triangular waveform OPD can be realized with perfect accuracy ( $\sigma_\phi = \pi/(4\sqrt{3})$  rad), we have derived  $V_{\text{red}}$  values of 0.99 and 0.90 for our optimized step pyramid and perfect triangle wave OPD modulation, respectively. For a given SNR, the increase in  $V$  (and hence  $V^2$ ) obtained by not scanning the fringes during the PSI measurements, but by stepping between four positions, thus corresponds to an effective sensitivity enhancement of 20%. Alternatively, this can be viewed as a limiting magnitude improvement of 0.2 magnitudes. We have assumed here a perfect triangle wave OPD and that the detector would be integrated for the entire period of the step pyramid. In practice however, a perfect triangle wave cannot be realized, and the inflection points will be rounded. During these inflection points, and likewise with the stepping points in the step pyramid, the integrated signal is discarded.

It is interesting to compare the residual OPD error from our  $K_S$  optimized step pyramid modulation scheme, shown in Fig. 10, to the temporal wavefront perturbations that might be expected to be introduced by the atmosphere during a few millisecond integration time. In Fig. 10, we have assumed that

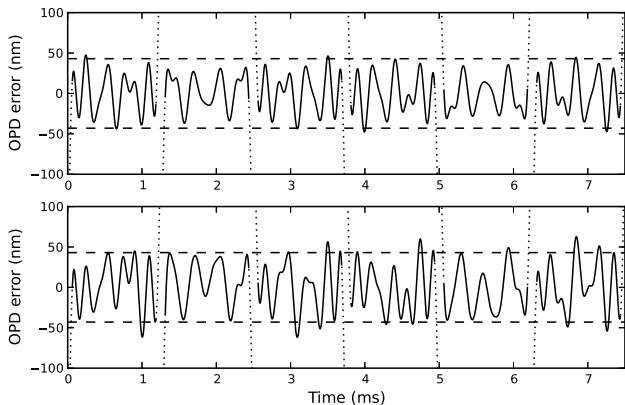


Fig. 10. Residual OPD error for step pyramid modulation appropriate to the  $K_S$  band (top) as measured by strain gauge measurements and (bottom) measurements with an external laser metrology system. The horizontal dashed lines represent a  $\lambda/50$  wavefront error for the  $K_S$  band, while the dashed portions of the OPD error correspond to those times during which the OPD is being stepped and the PSI data discarded. These times represent 10% of the entire modulation period. The OPD errors (excluding the dashed portions) have  $\sigma = 23$  nm and 28 nm for the top and bottom panels, respectively, resulting in  $\lambda/93$  and  $\lambda/77$  wavefront errors for the  $K_S$  waveband.

90% of the total period is used for integrating signal on the detector. The remaining 10%, shown as the intervals between vertical dotted lines, corresponds to the time during which the OPD is being rapidly stepped, and so the signal integrated during those times will not be of interest. The top panel in the figure shows the OPD error due to mirror motion inferred from the strain gauge data ( $\sigma = 23$  nm), while the bottom panel shows the OPD as inferred by the metrology system, which has  $\sigma = 28$  nm. These values correspond to wavefront errors of  $\lambda/93$  and  $\lambda/77$  for the top and bottom panels, respectively, in the  $2.15$   $\mu\text{m}$   $K_S$  band.

It has been shown at the VLTI that, for integration times of up to 8 ms on apertures of sizes similar to that of the MROI, and under excellent seeing conditions, one would expect an atmospheric piston error of no more than roughly  $\lambda/35$  to be introduced within an integration time in the  $1.65$   $\mu\text{m}$   $H$  band [33]. This equates to approximately  $\lambda/45$  in the  $2.15$   $\mu\text{m}$   $K_S$  band. The OPD errors introduced by our modulator are thus highly likely to be smaller than those introduced by the atmosphere, even under excellent and stable conditions, and so are consistent with the design framework of the MROI in which each subsystem has been designed such that any contributions to fringe coherence losses are maintained at a level smaller than those expected from residual atmosphere perturbations.

## 6. Conclusion

We have demonstrated a variety of OPD modulation strategies for rapid PSI measurements using an open-loop PZT-actuated modulator. By optimizing the driving waveform to the PZT actuator, we have been able to accommodate nonlinearities in the PZT and its associated optomechanics so as to deliver very well-defined OPD trajectories. Our tests have focused on continuous triangle and, more important, stepped-pyramid modulation schemes at frequencies above 100 Hz, i.e., higher than has been demonstrated with closed-loop controllers, but we expect that our scheme can be applied to a wide range of possible modulation types and frequencies.

We have found that our approach, using an iterative optimization of the open-loop PZT drive waveform, is rapid and reliable, and delivers an OPD waveform that is stable over long time scales. For low-light-level applications, such as astronomical interferometry where using some of the signal photons to monitor the modulator performance is not desirable, an open-loop solution such as the one we have demonstrated is likely to be very valuable.

In a PSI application specific to stellar interferometry, a 20% increase in the available SNR for fringe tracking was demonstrated. Equivalently, this corresponds to an enhancement in the limiting sensitivity of the fringe tracker of 0.2 magnitudes for a given SNR.

The authors thank Nicolas Torres, Victor Alvidrez, David Baird, Chuck Dahl, and Bodie Seneta for their

contributions and suggestions. The Magdalena Ridge Observatory was funded by Agreement No. N00173-01-2-C902 with the Naval Research Laboratory (NRL) and is funded through an institutional revenue bond from the New Mexico Institute of Mining and Technology (NMT). MROI is hosted by the NMT at Socorro, New Mexico, USA, in collaboration with the University of Cambridge (UK). Our collaborators at the University of Cambridge wish to also acknowledge their funding via STFC in the UK.

## References

1. A. J. Moore, R. McBride, J. S. Barton, and J. D. C. Jones, "Closed-loop phase stepping in a calibrated fiber-optic fringe projector for shape measurement," *Appl. Opt.* **41**, 3348–3354 (2002).
2. G. Li, Y. Li, K. Yang, and M. Liu, "A linearity tunable DBR fiber laser based on closed-loop PZT," *Opt. Laser Technol.* **45**, 702–704 (2013).
3. X.-j. Duan, F.-j. Duan, and C.-r. Lv, "Phase stabilizing method based on PTAC for fiber-optic interference fringe projection profilometry," *Opt. Laser Technol.* **47**, 137–143 (2013).
4. H. Jung, J. Y. Shim, and D. Gweon, "New open-loop actuating method of piezoelectric actuators for removing hysteresis and creep," *Rev. Sci. Instrum.* **71**, 3436–3440 (2000).
5. C. Ai and J. Wyant, "Effect of piezoelectric transducer nonlinearity on phase shift interferometry," *Appl. Opt.* **26**, 1112–1116 (1987).
6. J. D. Monnier, "Optical interferometry in astronomy," *Rep. Prog. Phys.* **66**, 789–857 (2003).
7. C. Haniff, "Ground-based optical interferometry: a practical primer," *New Astron. Rev.* **51**, 583–596 (2007).
8. E. Pedretti, W. A. Traub, J. D. Monnier, R. Millan-Gabet, N. P. Carleton, F. P. Schloerb, M. K. Brewer, J.-P. Berger, M. G. Lacasse, and S. Ragland, "Robust determination of optical path difference: fringe tracking at the Infrared Optical Telescope Array interferometer," *Appl. Opt.* **44**, 5173–5179 (2005).
9. J. D. Monnier, F. Baron, M. Anderson, S. Kraus, R. Millan-Gabet, E. Pedretti, X. Che, T. A. ten Brummelaar, and N. Calvet, "Tracking faint fringes with the CHARA-Michigan Phasetracker (CHAMP)," *Proc. SPIE* **8845**, 88451I (2012).
10. F. Cassaing, B. Fleury, C. Coudrain, P. Madec, E. di Folco, A. Glindemann, and S. A. Leveque, "Optimized fringe tracker for the VLTI/PRIMA instrument," *Proc. SPIE* **4006**, 152–163 (2000).
11. J. Sahlmann, S. Ménardi, M. Accardo, R. Abuter, S. Mottini, and F. Delplancke, "The PRIMA fringe sensor unit," *Astron. Astrophys.* **507**, 1739–1757 (2009).
12. T. A. ten Brummelaar, H. A. McAlister, S. T. Ridgway, W. G. Bagnuolo, Jr., N. H. Turner, L. Sturmman, J. Sturmman, D. H. Berger, C. E. Ogden, R. Cadman, W. I. Hartkopf, C. H. Hopper, and M. A. Shure, "First results from the CHARA Array. II. A description of the instrument," *Astrophys. J.* **628**, 453–465 (2005).
13. D. H. Berger, J. D. Monnier, R. Millan-Gabet, T. A. ten Brummelaar, P. Muirhead, E. Pedretti, and N. Thureau, "CHARA Michigan phase-tracker (CHAMP): design and fabrication," *Proc. SPIE* **6268**, 62683K (2006).
14. J.-B. Le Bouquin, R. Abuter, P. Haguenaue, B. Bauvire, D. Popovic, and E. Pozna, "Post-processing the VLTI fringe-tracking data: first measurements of stars," *Astron. Astrophys.* **493**, 747–752 (2009).
15. J. T. Armstrong, D. Mozurkewich, L. J. Rickard, D. J. Hutter, J. A. Benson, P. F. Bowers, N. M. Elias II, C. A. Hummel, K. J. Johnston, D. F. Buscher, J. H. Clark III, L. Ha, L.-C. Ling, N. M. White, and R. S. Simon, "The navy prototype optical interferometer," *Astrophys. J.* **496**, 550–571 (1998).
16. G. Vasisht and A. J. Booth, "Performance and verification of the Keck Interferometer fringe detection and tracking system," *Proc. SPIE* **4838**, 824 (2003).
17. M. M. Colavita, A. Booth, J. Garcia-Gathright, G. Vasisht, R. Johnson, and K. Summers, "Fringe measurement and control for the Keck Interferometer," *Publ. Astron. Soc. Pac.* **122**, 795–807 (2010).
18. M. M. Colavita, J. K. Wallace, B. E. Hines, Y. Gursel, F. Malbet, D. L. Palmer, X. P. Pan, M. Shao, J. W. Yu, A. F. Boden, P. J. Dumont, J. Gubler, C. D. Koresko, S. R. Kulkarni, B. F. Lane, D. W. Mobley, and G. T. van Belle, "The Palomar Testbed Interferometer," *Astrophys. J.* **510**, 505–521 (1999).
19. F. Bai, "Phase-shifts  $n\pi/2$  calibration method for phase-stepping interferometry," *Opt. Express* **17**, 16861–16868 (2009).
20. A. G. Basden and D. F. Buscher, "Improvements for group delay fringe tracking," *Mon. Not. R. Astron. Soc.* **357**, 656–668 (2005).
21. R. Langoju, A. Patil, and P. Rastogi, "Phase-shifting interferometry in the presence of nonlinear phase steps, harmonics, and noise," *Opt. Lett.* **31**, 1058–1060 (2006).
22. M. J. Creech-Eakman, V. Romero, I. Payne, C. Haniff, D. Buscher, C. Aitken, C. Anderson, E. Bakker, T. Coleman, C. Dahl, A. Farris, S. Jiminez, C. Jurgenson, R. King, D. Klinglesmith III, K. McCord, T. McCracken, K. Nyland, A. Olivares, M. Richmond, M. Romero, C. Salcido, J. Sandoval, F. Santoro, J. Seamons, R. Selina, A. Shtromberg, J. Stenson, N. Torres, D. Westpfahl, F. Baron, M. Fisher, E. Seneta, X. Sun, D. Wilson, and J. Young, "Magdalena Ridge Observatory Interferometer: advancing to first light and new science," *Proc. SPIE* **7734**, 773406 (2010).
23. C. A. Jurgenson, F. G. Santoro, F. Baron, K. McCord, E. K. Block, D. F. Buscher, C. A. Haniff, J. S. Young, T. A. Coleman, and M. J. Creech-Eakman, "Fringe tracking at the MROI," *Proc. SPIE* **7013**, 70131C (2008).
24. M. M. Colavita, B. E. Hines, and M. Shao, "A high speed optical delay line for stellar interferometry," in *European Southern Observatory Conference and Workshop Proceedings*, J. M. Beckers and F. Merkle, eds. (European Southern Observatory, 1992), Vol. **39**, p. 1143.
25. M. S. Fadali and A. Visioli, *Digital Control Engineering* (Academic, 2009).
26. L. Pickelmann, Piezomechanik GmbH, Berg am Laim Str. 64, D-81673 Munich (personal communication, 2013).
27. H. Thorsteinsson and D. F. Buscher, "A fast amplified fringe modulator and its waveform optimisation," *Proc. SPIE* **6268**, 626837 (2006).
28. A. M. Jorgensen, D. Mozurkewich, J. Murphy, M. Sapantaie, J. T. Armstrong, G. C. Gilbreath, R. Hindsley, T. A. Pauls, H. Schmitt, and D. J. Hutter, "Characterization of the NPOI fringe scanning stroke," *Proc. SPIE* **6268**, 62684A (2006).
29. T. Brummelaar, "Correlation measurement and group delay tracking in optical stellar interferometry with a noisy detector," *Mon. Not. R. Astron. Soc.* **285**, 135–150 (1997).
30. D. F. Buscher, "Getting the most out of COAST," Ph.D. dissertation (University of Cambridge, 1988).
31. M. M. Colavita, "Fringe visibility estimators for the Palomar Testbed Interferometer," *Publ. Astron. Soc. Pac.* **111**, 111–117 (1999).
32. I. L. Porro, W. A. Traub, and N. P. Carleton, "Effect of telescope alignment on a stellar interferometer," *Appl. Opt.* **38**, 6055–6067 (1999).
33. N. Blind, O. Absil, J. L. Bouquin, J. Berger, and A. Chelli, "Optimized fringe sensors for the VLTI next generation instruments," *Astron. Astrophys.* **530**, A121 (2011).